Low-Dimensional, Hinged Bar-code Metal Oxide Layers and Free-Standing, Ordered Organic Nanostructures from Turbostratic Vanadium Oxide

Colm O'Dwyer, Vladimir Lavayen, David Fuenzalida, Harold Lozano, Maria A. Santa Ana, Eglantina Benavente, Guillermo González, and Clivia M. Sotomayor Torres*

***B**oth low-dimensional bar-coded metal oxide layers, which exhibit molecular hinging, and free-standing organic nanostructures can be obtained from unique nanofibers of vanadium oxide (VO_x). The nanofibers are successfully synthesized by a simple chemical route using an ethanolic solution of vanadium pentoxide xerogel and dodecanethiol resulting in a double bilayered laminar turbostratic structure. The formation of vanadium oxide nanofibers is observed after hydrothermal treatment of the thiol-intercalated xerogel, resulting in typical lengths in the range 2–6 μm and widths of about 50–500 nm. We observe concomitant hinging of the flexible nanofiber lamina at periodic hinge points in the final product on both the nanoscale and molecular level. Bar-coded nanofibers comprise alternating segments of organic–inorganic (thiols–VO_x) material and are amenable to segmented, localized metal nanoparticle docking. Under certain conditions free-standing bilayered organic nanostructures are realized.*

Keywords:
- hydrothermal synthesis
- intercalation
- nanofibers
- organic–inorganic composites

[*] Dr. C. O'Dwyer[+]
Tyndall National Institute
University College Cork
Lee Maltings, Cork (Ireland)
Fax: (+353) 21 490-4467
E-mail: colm.odwyer@ul.ie

Dr. V. Lavayen[++], D. Fuenzalida, H. Lozano, Dr. M. A. Santa Ana, Prof. G. González
Department of Chemistry, Faculty of Science
Universidad de Chile
Santiago (Chile)

Prof. E. Benavente
Department of Chemistry
Universidad Tecnológica Metropolitana
Santiago (Chile)

Prof. C. M. Sotomayor Torres
Institute for Research and Advanced Studies, ICREA
08010 Barcelona (Spain)

Prof. C. M. Sotomayor Torres
Catalan Institute of Nanotechnology, Edifici CM7
Campus Universitat Autonoma de Barcelona
08193 Bellaterra, Barcelona (Spain)

[+] Present address: Department of Physics, and Materials and Surface Science Institute, University of Limerick, Limerick, Ireland.

[++] Present address: Área de Ciências Naturais e Tecnológicas, Centro Universitário Franciscano, Santa Maria, Rio Grande do Sul, CEP 97010-032, Brazil.

1. Introduction

One-dimensional nanomaterials, such as nanotubes,[1] nanowires,[2–4] and nanobelts or nanoribbons,[5,6] have attracted considerable attention in the past decade because of their novel and useful physical properties, leading to numerous applications. Besides the use of 1D metal oxide nanostructures as functional components in electronics and interconnects in dense, high-speed integrated circuits, they also find application in ultrasmall sensors, optical elements for optoelectronics, nonlinear optical converters, and information storage devices.[7,8] Because of the versatile chemical properties often moldable by changes in the oxidation state of the metal coordination sphere and a judicious choice of intercalating organic guest molecules, metal oxide nanostructures may lead to a variety of products and tuneable materials.[9,10] Vanadium oxide has attracted considerable attention as a Li^+ intercalation host, because of its layered structure, and also, depending on the nature of the species present in the reaction medium, vanadium oxides may exhibit a wide range of morphologies. Nanostructures such as lamellae,[8] scrolled nanotubes,[11,12] nanowires,[13] nanorods,[14] and nanourchin[15,16] have been realized using a variety of organic templates during synthesis. Each of these structures

relies on the structural direction provided by intercalated or adsorbed organic molecules.

The interest in the role of membrane curvature is profound; its understanding is only starting to become important in nanobiological materials because of the ubiquitous nature of curved lipid layers/membranes in living systems[17,18] and because it results in unique nanotubular structures from curved lamellar metal oxides. The curvature can have a significant effect on the bilayer structure, and recent experiments demonstrated curvature-directed segregation of lipid mixtures in nonplanar membranes.[19,20] The need to understand how curvature is induced and affects the physical properties of layers and membranes is crucial in such systems.[21,22] When the main body of a nanostructure, such as lamellar vanadium oxide nanofibers, comprises longitudinally segmented sections, these heterostructured nanofibers can provide bar code-like docking points for a wide range of moieties, such as functionalizable organic ligands and metal or optically active nanoparticle incorporation.[12] Each segment can thus serve as a recognition site or adsorption region. This attribute, among many others, accounts for the growing interest in bar-coded layered materials in bioanalytics, diagnostics, and separation, for example,[23,24] and even opportunities for assembling functional architectures with lipid-membrane- mediated biorecognition.[25] End-, side-, and segment-specific molecular recognition can facilitate end-to-end, side-to-side, and end-to-side assembly of different nanostructural architectures, such as chains, bundles, and crossbars by taking advantage of, for example, magnetic interactions with susceptible metal nanoparticles in the intersegment voids.

The advantage of template-based growth methods is the ability of fabricating unidirectionally aligned and uniformly sized nanostructured arrays, and further study and development of template-based growth of prospective multifunctional nanostructures is obviously of significant importance. Because of the high efficiency, simplicity and, versatility of their synthesis, bottom-up approaches using surfactants or micelles as the regulating structural directors or templates can be readily employed in the fabrication of low-dimensional nanostructures. Recent developments in chemical nanolocomotion have raised the intriguing possibility of assembling nanomachines with metal nanorods;[26,27] nanostructured constructs displaying any form of flexibility of discrete compositional variations along their length are only beginning to be discovered.[28] Further scientific and technological advances in the application of low-dimensional nanostructures in functional devices depend on the ability to organize them[29] in complex one- or multi-dimensional functional architectures.

Here, we detail the successful synthesis and realization of multifunctional laminar vanadium oxide intercalates. This turbostratic thiol-functionalized VO_x nanofiber exhibits morphological variations, such as periodic bar coding by longitudinal modulation of the metal oxide caused by periodic organic– inorganic segmentation, delamination to form free-standing molecular bilayer films, and curvature-induced hinging under hydrothermal conditions on the nanoscale and molecular level.

2. Results and Discussion

2.1. Thiol-Templated and Structurally Directed Bilayered VO_x Nanocomposite

The formation of vanadium oxide nanofibers was achieved by hydrothermal treatment of the precursor composed of vanadium pentoxide xerogel $V_2O_5 \cdot nH_2O$ and dodecanethiol (DDT), resulting in an inorganic–organic laminar VO_x-$(DDT)_{0.27}$ nanocomposite. The powder X-ray diffraction (XRD) patterns of both the xerogel and the nanocomposite prior to hydrothermal treatment (HT) are shown in Figure 1a. We observe that VO_x-$(DDT)_{0.27}$ exhibits a set of {00*l*} peaks characteristic of the formation of a bilayer laminar phase and evidence for the formation of a crystalline matrix.

The interlaminar distance is measured to be 2.5 nm from the (001) Bragg reflection of the nanocomposite. The degree of laminar crystallinity is reflected by the observation of eleventh order {00*l*} reflections for this composite within the experi-

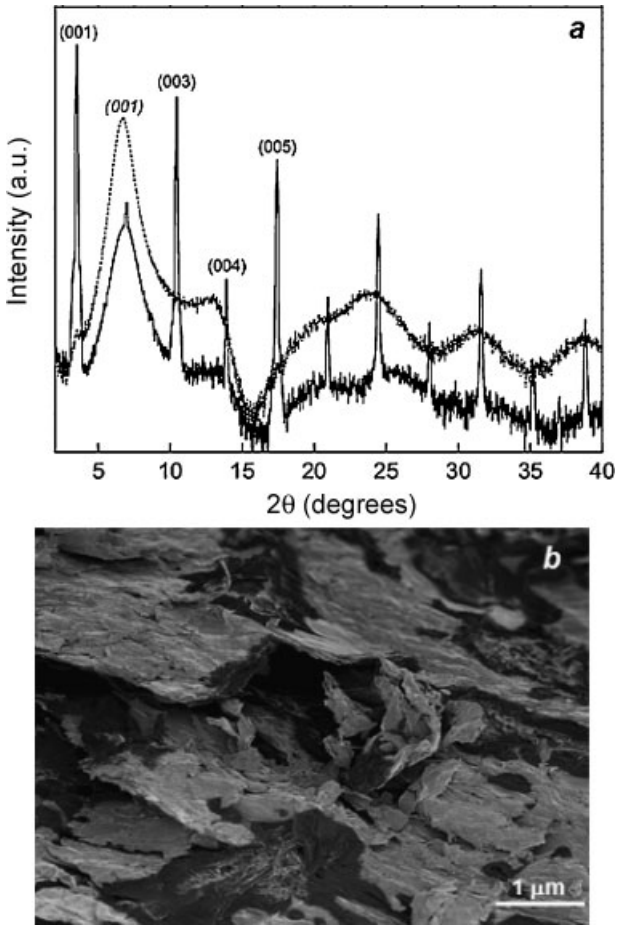

Figure 1. a) Powder X-ray diffraction (XRD) patterns of the VO_x-$(DDT)_{0.27}$ nanocomposite (solid line) product prior to hydrothermal treatment (HT) and the $V_2O_5 \cdot nH_2O$ xerogel (dashed line). The diffraction peaks were indexed on the basis of a two-dimensional square lattice with $a = 0.611$ nm, indicating high structural order of the thiol–vanadate bilayers. b) Field-emission scanning electron microscopy (FESEM) image of the VO_x-$(DDT)_{0.27}$ nanocomposite product prior to HT, showing its bulk laminarity.

mental 2θ range of 0°–40°. By comparison, the interlaminar spacing of the monoclinic ($a_0 = 1.1964$ nm, $b_0 = 0.4697$ nm, $c_0 = 0.5324$ nm; space group = $c2/c$) $V_2O_5 \cdot nH_2O$ xerogel is calculated to be 1.27 nm from its respective (001) Bragg reflection and displays a lower degree of long-range laminarity. The diffraction pattern for the nanocomposite is consistent with the intercalation of the thiol surfactant template into the laminar matrix and indicates that the framework of the host xerogel is preserved, coherent with a topotactic reaction. In particular, the structure permits thiol molecules to be embedded between the layers in an ordered fashion, leading to the formation of the quasi-crystalline VO_x-$(DDT)_{0.27}$ phase. The laminar morphology of the product is clearly observed even on the macroscale as evidenced by the field-emission scanning electron microscopy (FESEM) image of the product (Figure 1b). It is apparent from the micrograph that the overall morphology is that of a bulk laminar compound.

There is a notable absence of a high intensity (002) reflection in the xerogel diffraction pattern (both curves in Figure 1a are plotted on a semi-logarithmic scale), consistent with its arrangement as a double bilayered product where two vanadate layers are bound by a bilayered surfactant[7,16] and this arrangement is stacked periodically back-to-back. We also observe similarly low intensities for the {00l} peaks, where $l = 2, 4, 6, \ldots, 2(n-1)$; $n \in \aleph$.

The measured interlaminar distance of 2.5 nm, which is larger than the dodecanethiol molecular length ($CH_3(CH_2)_{11}SH \approx 1.87$ nm), implies a double layer of the thiol, oriented either perpendicular to the VO_x planes with interdigitated alkyl chains or forming an angle with them, as previously reported.[16] The values suggest that the intercalated surfactant adopts a tilted bilayer structure, a well-documented ordering for self-assembled monolayers of thiols.[30,31]

XRD analysis was also conducted on the nanocomposite after HT, as observed in the diffraction pattern in Figure 2. Heat treatment of the reaction mixture leads to the formation of a pure mesophase comprising a laminar species (see below) that exhibits two phases: one with an overall laminar distance of 4.9 nm, identified as orthorhombic V_2O_5[32] and a second phase that exhibits a laminar tendency with an associated laminar thickness of 3.9 nm. As observed for the vanadate lamina, a low (002) diffraction intensity confirms the bilayered structure of the intercalated organic layer. The second phase is identified as the thiol surfactant bilayer, the theoretical bilayer length of which (as measured from two juxtaposed head–tail molecules) is 3.74 nm. The high intensity phase (indicated by * in Figure 2) thus has the value of 4.9 nm for the overall interlaminar spacing of the nanocomposite and that of the interlaminar length of the surfactant.[33] The difference between measured and theoretical molecular bilayers' length is due to the well-documented uptake of water molecules[34] within the vanadate lamina of the xerogel verified here from Fourier transform infrared (FTIR) measurements, as outlined below.

The IR vibrational spectrum obtained for the laminar VO_x-$(DDT)_{0.27}$ nanofibers (Figure 3) highlights key vibrational characteristics of the intercalated lamina; by comparison, previous reports[35] have shown that the V_2O_5 xerogel displays three principal absorption peaks at 530, 765, and

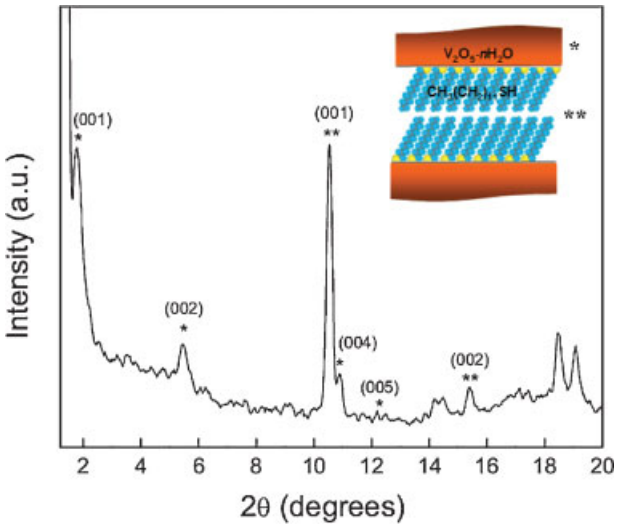

Figure 2. Powder XRD pattern of the VO_x-$(DDT)_{0.27}$ nanocomposite product after HT. Bilaminar diffraction from the vanadium oxide nanofibers is indicated by *. The diffraction contribution from the intercalated organic bilayer is indicated by **. The inset shows a schematic of the double bilayered system, highlighting each bilaminar region contributing to the diffraction pattern.

1012 cm^{-1}. The FTIR measurements in Figure 3, however, exhibit four characteristic vibrational bands. Spectral analysis shows that these frequencies correspond to the V=O bond of the vanadyl oxygen at about 1008 cm^{-1}, a wide asymmetric V–O–V stretching band with a maximum at 756 cm^{-1}, and a symmetric V–O–V stretching (525 cm^{-1}) mixed with deformation vibrations of the vanadium–oxygen polyhedra.[36]

As stated, the band at 1008 cm^{-1} corresponds to the vibrational V=O stretching mode; we have estimated interatomic distances in this wavenumber range that correspond to the presence of the distorted pentavalent orthor-

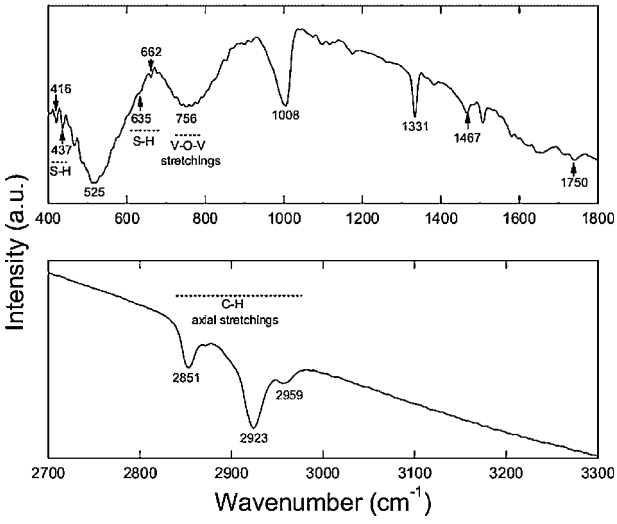

Figure 3. FTIR transmittance spectrum, averaged from 300 scans, of the VO_x-$(DDT)_{0.27}$ nanocomposite product after HT. The spectra were acquired from bulk samples of nanofibers with different respective orientations to the incident probe beam.

hombic γ-V_2O_5 conformation, yielding an associated V=O bond length of 0.155 nm.[11] This observation implies that a distortion of the monoclinic vanadate lamina, by deformation of the vanadium–oxygen polyhedra, to that of orthorhombic vanadate occurs during HT and is influenced by the presence of the thiol molecular template. The nanotube walls are composed of vanadium oxo-anions with either a neutral or negative charge. If present, the V^{5+} neutralizes this charge; V^{4+} does not. Consequently, the total anion charge on the nanotube walls is a direct function of the V^{4+} content. As the thiol surfactant used in this work is the structural template and is also anionic, greater quantities of V^{4+} does not necessarily result in more surfactant binding. As the associated electrostatic interaction is much stronger than dative bonding between neutral V^{5+} sites and amine head groups,[37] select areas on any nanofibers that contain high quantities of quadravalent vanadium are thus susceptible to delamination because of reduced surfactant–vanadate binding interactions.

Intense bands resulting directly from surfactant molecules are observed at 2959, 2923, and 2851 cm^{-1}, and are related to the axial stretching of the aliphatic C–H bond of the methyl and methylene groups. Vibrational spectroscopy has been used extensively to probe the conformation and organization of alkyl chain assemblies. The frequency and line shape of the stretching and bending vibrational modes of the CH_2 and CH_3 groups are sensitive to the gauche-to-trans conformer ratio of the alkyl chains. The methylene stretching modes, for example, shift from lower frequencies, characteristic of the highly ordered all-trans conformation, to higher frequencies and increased line-width as the number of gauche conformers in the chain increases. For an all-trans alkyl chain, as in the case of crystalline *n*-alkanes, the symmetric and antisymmetric stretching frequencies are typically in the range 2846–2849 and 2916–2919 cm^{-1}, respectively.[38] With a greater number of gauche defects this range blue-shifts to 2850–2854 and 2921–2925 cm^{-1}, respectively, as observed in Figure 3. These spectroscopic observations show that even in the absence of intermolecular interactions, weak adhesive interactions are sufficient to cause methylene chains to adopt an all-trans (solid-like) configuration in the vicinity of a confining surface while accommodating a low density of alkyl chains with gauche defect (liquid-like) conformations. A detectable gauche-defect vibrational contribution to the measured signal can only indicate a greater freedom of movement of the interlayer methylene groups resulting from a less-ordered packing of the thiols; hinging, bending, and shearing are potentially allowed.

Other notable bands are located at 1467 cm^{-1}, related to in-plane symmetric angular deformations of the CH_2 groups, as well as a relatively weak band at 721 cm^{-1}, corresponding to the C–H bending mode of the methylene groups in the surfactant template. The H–O–H vibrational modes typically found[39] in the wavenumber region 3890–3640 cm^{-1} were not observed; however, a weak signal with a maximum at 1750 cm^{-1} indicates a detectable presence of remnant water molecules within the VO_x-$(DDT)_{0.27}$ nanocomposite[40] after HT.

The presence of the lateral S–H stretching vibration mode is not detected in the range 2600–2550 cm^{-1}, but between 700–600 cm^{-1} we observe very weak signals from the C–S stretching vibration mode at 662 and 635 cm^{-1}. The absence of the lateral stretching mode and the weakness in intensity of the vertical stretching modes indicate solid confinement and adsorption within the interlaminar spacing and almost no detectable 'wiggle' of the alkyl-chain head group at the adsorption site. Structural defects are confined between the center and tail of the alkyl chain.

2.2. Turbostratic Bar-coded Inorganic–Organic Morphology and Molecular Hinging

Further structural characterization of the nanofibers was performed using transmission electron microscopy (TEM), as shown in the low-magnification TEM images of Figure 4a and b, giving the nanofibers with different respective orientations, that is, side- and plan-view perspectives. The measurements reveal that the high-aspect-ratio nanofibers of vanadium pentoxide have lengths typically in the range 2–6 μm and plan-view widths in the range 50–500 nm. A feature common to all synthesized nanofibers is the quasi-periodic hinging points perpendicular to the long axis of the fiber (Figure 4b) and the zig-zag nanofibers, seen in Figure 4a, formed by segments of the nanofibers having their long axes at different respective angular positions. Selected-area electron diffraction (SAED) measurements (Figure 4b, inset) indicate that the vanadate constituent of the fibers is orthorhombic V_2O_5 with reconstructed lattice parameters of $a_0 = 1.152$ nm, $b_0 = 0.356$ nm, $c_0 = 0.437$ nm; space group = *Pmnm*. The bulk electron diffraction (ED) pattern shows prominent polycrystalline diffraction rings (1, 2, and 3) with *d*-spacings matching the (200), (001), and (110) reflections of orthorhombic V_2O_5. We also observe longitudinal bar-coded morphology with intermittent inorganic and organic segments (Figure 4c). As will be clarified in the next Section, the organic segments are pristine bilayers of alkanethiols and the alternating dark regions (in Figure 4c) are vanadium oxide lamina.

In an aqueous HT environment, these nanorods display Brownian-type bending movements of metal oxide segments about the flexible hinges on both the nanoscale and at a molecular level, as shown in Figure 5. The fabrication of nanoscale flexible hinges between vanadium oxide segments was accomplished by utilizing the layer-by-layer electrostatic self-assembly of the turbostratic thiol-intercalated VO_x nanofibers. It represents an inherent improvement to the synthetic method described by Yu et al.,[41] where charged nanorods are entirely encapsulated with polyelectrolytes through layer-by-layer electrostatic self-assembly.[42] Their approach entails iterative dipping of the charged nanorods in alternating baths of positive and negative polyelectrolytes to create encapsulating polymeric sheaths, beginning with a monolayer and building up to a predetermined thickness with multiple layers. In this work, a new approach that incorporates the 'sheathing' steps is achieved during the formation of the organic–inorganic multilayered xerogel. The thiol template acts as a soft polymer sheath under nanometer thickness control facilitating flexural motion. A series of TEM images was acquired immediately after HT (Figure 5, top) and

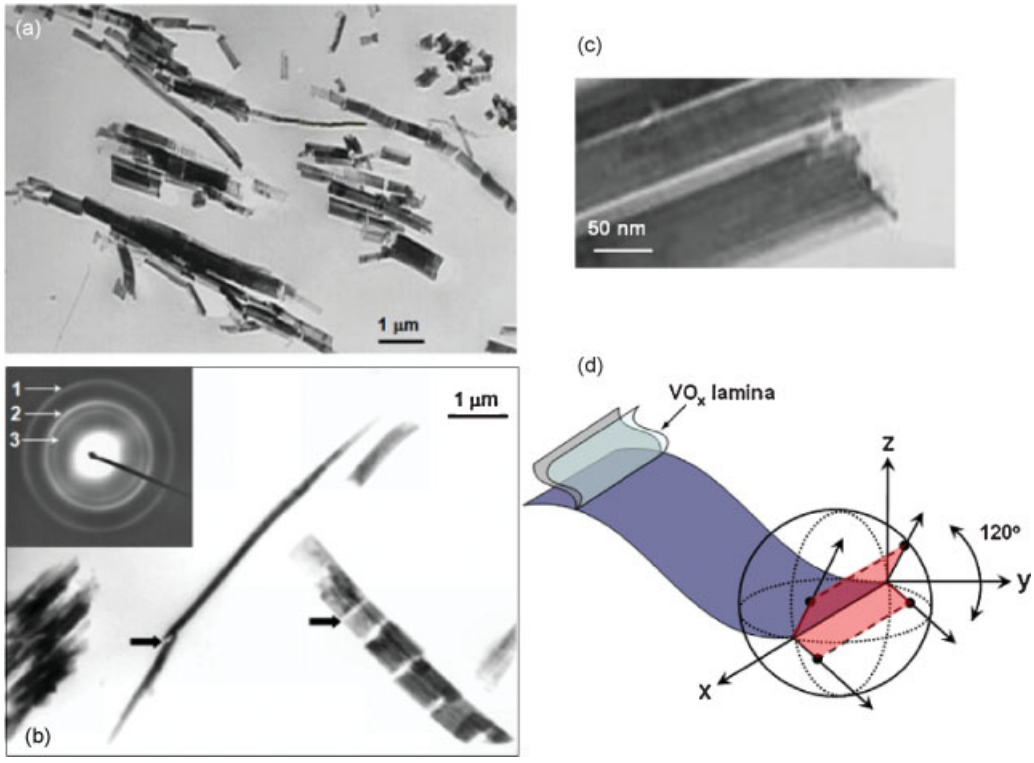

Figure 4. a) Bright-field TEM image of fully developed, bulk, multilayer VO_x-$(DDT)_{0.27}$ nanofibers upon cooling to room temperature after HT. b) TEM image of the plan- and side-view profiles of the nanofibers. Arrows in (b) highlight hinge points. The associated bulk electron diffraction pattern of the nanofibers is given in the inset. c) Cross-sectional TEM image of a nanofiber, highlighting the organic (bright)–inorganic (dark) bar-coded biphasic structure. d) Schematic representation of the observed hinging and bending vectors of the nanofiber lamina.

shows the bidirectional flexing of the nanoscale hinges, which are observed to flex back and forth. The position of the sample cross section with respect to the incident beam was optimized for perpendicularity by equalizing the electron diffraction contribution. In this series of images, we observe laminar bending or hinging where the vanadate lamina is observed to flex by approximately $\pm 60^\circ$. This flexural movement is outlined schematically in Figure 4d. For nanoscale hinges, no lateral or twisting motion of the nanofibers was observed, limiting the movement to the z-direction (Figure 4d) perpendicular to the VO_x lamina.

On the molecular level, we also observe displacement in the form of bidirectional bending of lamina only several molecular units thick (Figure 5, lower images). This series of images shows small-amplitude harmonic-like flexural motion of three double bilayers of thiol-intercalated vanadium oxide. The cross-sectional TEM images again show a limited angular range of motion, to one that is perpendicular to the laminar face. A total angular displacement of approximately $\pm 18^\circ$ is observed for the fiber segment.

These observations suggest that the relatively small-amplitude stochastic swings of the vanadium oxide segments are superimposed on a random translational Brownian-like motion of the bulk nanofibers. These results suggest that the mechanical stiffness of a hinge composed of multiple bilayers is sufficient to overcome the various forces that contribute to out-of-plane bending motion of the nanofiber. A single bilayer allows the nanofiber to undergo bending vibrations about the hinge. It is quite remarkable that such a thin molecular hinge is mechanically robust enough to support such large-amplitude bending motions. Over several hours, the process was monitored and no disruption (breakage or shearing) of the hinged nanofiber was observed.

In the two examples shown, the lengths of the segments and hinges are different, thereby providing an opportunity to observe whether such alterations in the architecture of hinged nanofibers influence their movement. This seems to be the case; further work along these lines is currently in progress in order to explore the system in greater detail to further support the integration of a functional hinge into multisegmented nanofibers.

To examine the coding capacity of the multisegmented bar-coded nanofibers, Au nanoparticle colloids prepared by chemical liquid deposition, were refluxed with the nanocomposite in an ethanol solution as described elsewhere.[12] In the bright- and dark-field TEM images shown in Figure 6a and b, respectively, the presence of the Au nanoparticles is not clearly visible in the former but, by employing dark-field imaging of the Au{111} reflection, brilliant points (Au nanoparticles) can be readily observed in the latter image, in the regions corresponding to those of lower diffraction contrast in Figure 6a. This observation indicates the preferential uptake of Au nanoparticles in the vicinity of the thiols, which is due to the affinity between Au and the S-containing head groups.

The system is thus amenable to guest-molecule/entity uptake or docking at predetermined sites on the host lamellar nanomaterial. Obvious extensions to this would be the

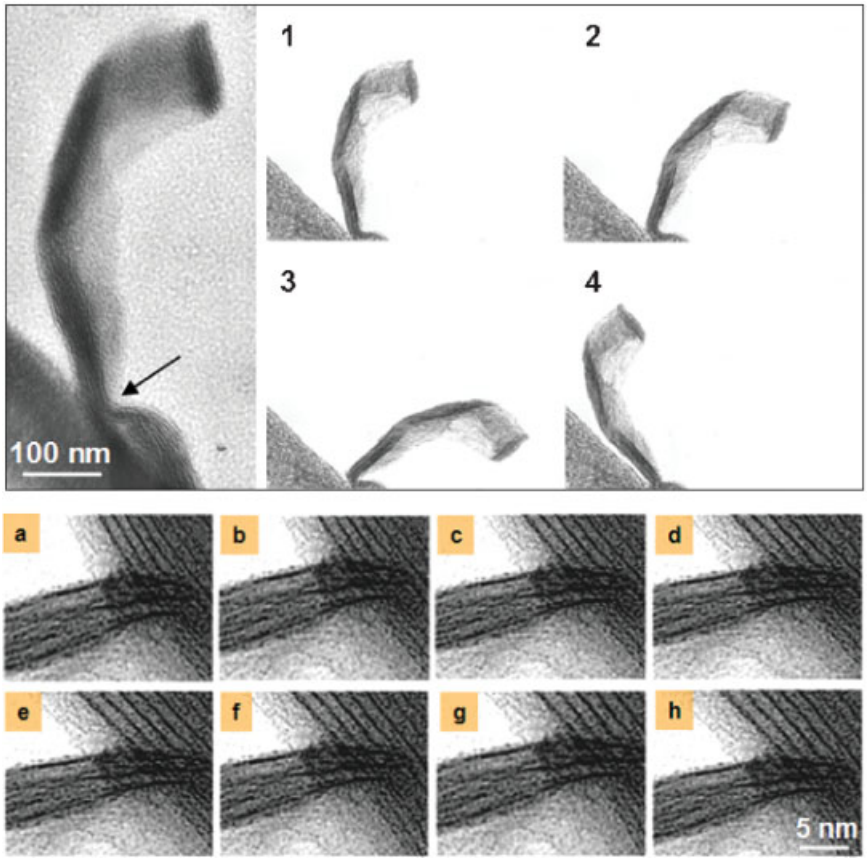

Figure 5. Top: A series of TEM snap-shot images of VO_x-$(DDT)_{0.27}$ nanofiber lamina. Lattice planes are clearly resolved through diffraction contrast. The pronounced turbostratic hinge point is highlighted by an arrow and was observed to undergo large-amplitude hinging as shown in images 1–4. Bottom: A series of high-resolution TEM images showing flexural hinged motion at the molecular level. The images show flexing and hinging with a maximum angular divergence of 18°. The hinging is observed from 65° (a) to 47° (e), and back to 63° (h).

bar-coded arrangement of luminescent dots, semiconducting nanocrystals, biological species, and so on, all of which are detectable through either microscopical, chemical, or non-destructive optical techniques.[43]

2.3. Free-Standing Ordered Organic Nanostructures

After hydrothermal treatment, we noted the unique formation of organic nanofibers and nanotubes in addition to the metal oxide nanofibers. These structures are observed to always stem from highly bar-coded organic–inorganic nanofibers, such as those in Figure 7a. Bilayered dodecanethiol nanofibers are observed in the higher magnification image of Figure 7b. Organic nanostructures observed in this work have typical diameters/widths of approximately 25 nm and they do not collapse under electron-beam irradiation. It is of interest to note that the thiols, normally resident between the vanadate layers, delaminate (observable at several areas in Figure 7a) and become freely susceptible to bending and subsequent removal during HT in some cases.

The possibility of realizing low-dimensional organic nanostructures is a novel advance considering that, until now, only insoluble amorphous powders are actually obtained by usual electrochemical or chemical oxidation of the corresponding monomers. In cases where organic nanostructures, caused by delamination, are observed, free-standing individual organic nanofibers and nanotubes are seen. Energy dispersive X-ray (EDX) spectroscopy measurements (Figure 7c) of the organic nanostructure in Figure 7b confirm the presence of thiols outside the main nanofiber structure by detection of the C content of the alkyl chains.

X-ray photoelectron spectroscopy (XPS) measurements were conducted on individual organic nanostructures to confirm the presence of sulphur from the thiol head groups and to derive semi-quantitative information on the S ordering as the outer 'skin' of the nanostructure. In the S 2p spectra (Figure 7d), a S 2p doublet at binding energies of approximately 162.0 and 163.2 eV (S $2p_{3/2}$ and S $2p_{1/2}$, respectively) is observed and is related to the bound thiolate species. The low signal-to-noise ratio of the S 2p spectra is related to the shortened acquisition time chosen to minimize any potential X-ray-induced damage during the measurement. The positions and full widths at half-maximum (ca. 1.2 eV) of the S $2p_{3/2}$ and S $2p_{1/2}$ peaks are essentially equivalent to those for conventional self assembled monolayers of alkanethiols.[44] Thus, the upper surface of the thiol nanostructure (Figure 7c) is similar to a monolayer of thiols where all the S-containing head groups reside on the outside of the structure (also depicted schematically in Figure 7b). Indeed, dedicated scanning tunnelling microscopy (STM) measurements (Figure 7e) were acquired on the organic segment of a side-view bar-coded nanofiber. The upper left of the image is the vanadium oxide and a neighboring double bilayered arrangement of the intercalated thiols is confirmed. It is most likely that the free-standing thiol nanostructures have a similar structure, although further work is required to determine whether the ordered organic structure is either a straight laminar bilayer or a bilayered helical architecture, both of which exhibit similar outer 'skins' of S-containing groups.

2.4. Defects causing Molecular Hinging, Laminar Bending and Bar-coded Morphology

A series of TEM images was also acquired at specific breakage points, previously seen highlighted in Figure 4b. In addition to determining the preferential growth direction of

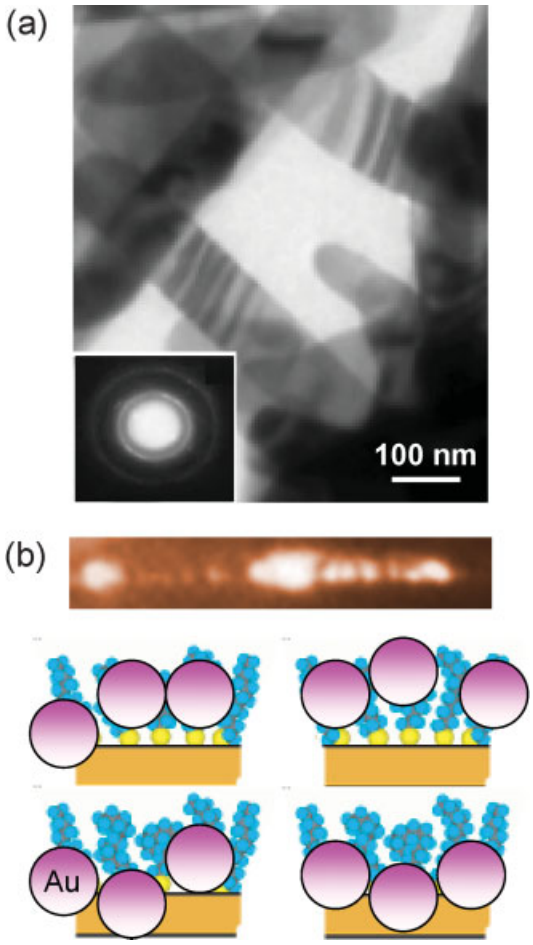

Figure 6. a) Bright-field TEM image of VO_x-$(DDT)_{0.27}$ nanofibers with longitudinal organic–inorganic bar-coded segmentation. An SAED pattern from a Au-nanoparticle-infiltrated nanofiber is shown in the inset, where the (111) and (220) reflections of Au can be seen. b) Higher magnification dark-field TEM image acquired at the Au{111} reflection. The brilliant areas represent Au nanoparticle colloids located in the vicinity of the organic bar code segments of the nanofibers, as outlined schematically underneath.

the fibers, we also observe that the hinges stem from polymorphic deformation on the atomic scale by either cleaving of the fiber cross sections, as seen at point K in Figure 8a, or buckling of the lamina, as seen at T (Figure 8b). The SAED pattern shown in Figure 8c is taken from a single nanofiber and recorded from the [100] zone axis, evidencing that the nanofibers are single crystals with a preferential growth direction along the [010] direction, layer-by-layer in the (*a*,*c*) planes. We note that, on either side of breakage points, it is the vanadate layer that undergoes atomic 'ripping' although the interlaminar distance and ordering remain intact throughout. It is these particular types of defects within the vanadate lamina that allow for the bar-coded inorganic–organic periodic morphology through delamination. It is further plausible that a similar mechanism is enhanced by evaporative drying after HT; the associated shrinkage would pronounce the cleaved areas to cause delamination facilitated by breakage and/or shearing-induced mechanical strain desorption of otherwise rigidly bound thiol head groups.

We also note that, in Figure 8b, the regions highlighted by ovals are where thiols have selectively delaminated and spread to the outer edge of the nanostructure, as evidenced by the reduced diffraction-contrast features. Because the amplitude and phase changes that occur when an electron is scattered elastically are characteristic of the atomic number, there will be changes in the elastic scattering directly related to the form of the projected scattering potential when there is a composition change at an interface viewed in projection by TEM, analogous to a phase-grating filtering of the scattered electronic wave function.

The gaps in the atomic layers are devoid of the heavier S-containing scattering centers as well as local voids in the vanadium oxide molecular layers. Individual atomic-layer bending is observed (Figure 8d) with bunched areas of locally high packing densities of S-containing head groups at the bend points, as evidenced through diffraction contrast. In Figure 8d, we also observe a shearing of the hinge point in lamina with large curvature at point S; to accommodate sufficient curvature to form an orthogonal bend in the overall nanofiber, shearing of the hinges occurs along the slip direction of the lamina and not out-of-plane angular slide motion, as depicted in the schematic in Figure 8.

In this example, hinging due to buckling is further evidence of the rigidity of the thiol-templated nanofibers compared to their amine-intercalated counterparts that undergo bending and scrolling deformations during HT to form tubular nanostructures.[15] Pristine monocrystalline nanofibers are observed to grow lengthwise and the subsequent back-to-back self-assembly results in the overall fiber morphology. It is noteworthy that, even when the increased rigidity of thiol-functionalized vanadate layers as opposed to those intercalated with alkyl amines is considered, the increase in interlaminar distance of the nanocomposite (from 2.5 to 4.9 nm as per the diffraction data) after HT must allow for some freedom of movement of the surfactant template to allow bending and breakage, possibly because of a lower degree of alkyl chain interdigitation and interaction. In fact, the degree of bilayered turbostratic laminarity and crystallinity of both the organic and inorganic phases is so pronounced that half-spacings (diffraction from the thiol bilayer within the vanadium oxide bilayer) are also observed in the SAED pattern in Figure 8c. The rigidity is directly due to an ordered molecular template; however, the measurable amount of movement within the bilayer itself contributes to the polymorphism and breakage observed in the nanofibers.

The $V_2O_5 \cdot nH_2O$ xerogel is essentially a stack of ribbon-like slabs that are layers of single V_2O_5 lamina that consist of edge-shared square pyramidal VO_5 units, amenable to polymorphic distortion and curving. These 2D sheets are weakly bound by van der Waals forces and are readily propped open by intercalation species such as dodecanethiol in this instance. Hydrothermal treatment of the thiol-containing xerogel induces loss of bound water molecules (removal of V–OH bonds) and recrystallization of the material to orthorhombic V_2O_5 during thiol bond-weakening,[45] corroborating the measured increase in overall interlaminar distance and explaining the allowance of delamination. Below circa 300 K, the system is in an orientationally ordered

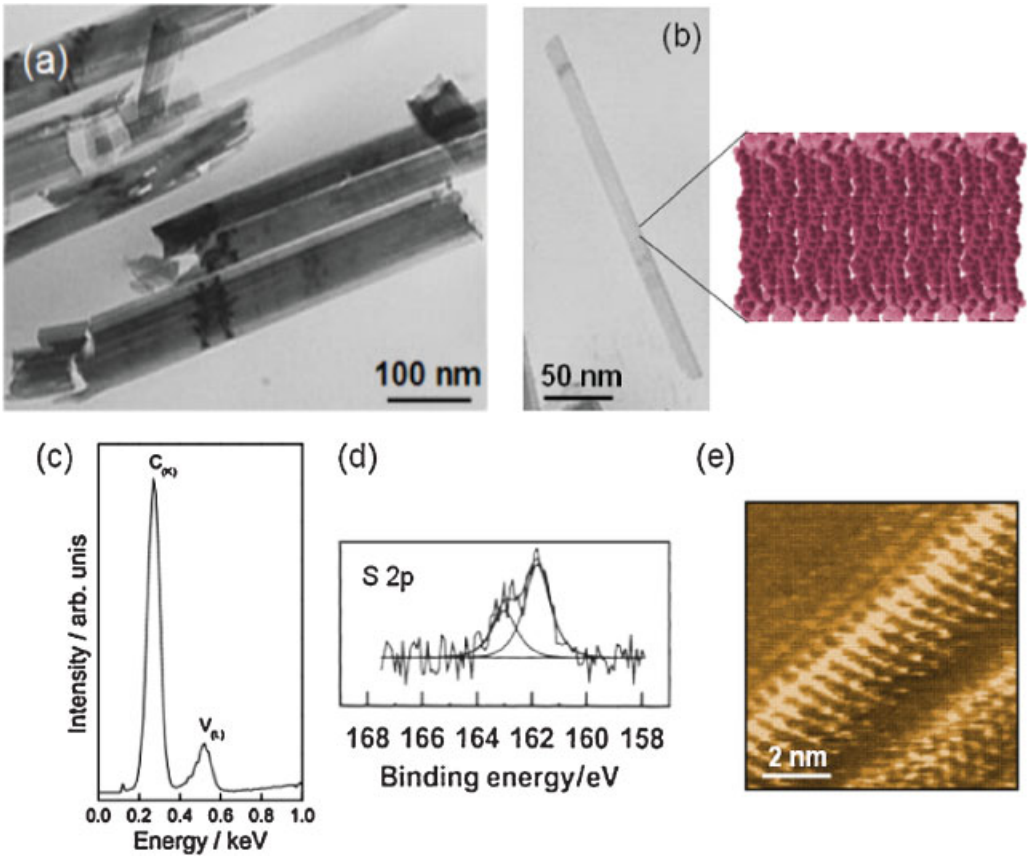

Figure 7. a) Bright-field TEM image of VO_x-$(DDT)_{0.27}$ nanofibers with longitudinal organic–inorganic bar-coded morphology. b) Higher magnification TEM image showing a single organic nanotube. Such structures have typical diameters/widths of about 25 nm. c) Energy dispersive X-ray spectrum of an organic nanotube showing the carbon K line and vanadium L line. d) S 2p X-ray photoelectron spectroscopy of the organic nanotubes. The observed emission structures are fitted by a doublet Voigt function (with fixed intensity ratio of S $2p_{3/2}$/S $2p_{1/2} = 2$ and a hyperfine splitting energy separation of 1.2 eV) related to the pristine thiolate moieties. e) 8 nm × 8 nm molecular-resolution scanning tunneling microscopy image of neighboring inorganic–organic segments of a nanofiber cross section in constant height mode with a sample bias of 1.5 V. Individual thiol molecules can be resolved.

crystalline phase. Between 300 and 370 K, it has been observed[46] that the surfactant gradually looses tilt as the temperature increases and the chains behave as hindered rotators. Above 370 K, the chains rotate more freely around their long axes and gauche defects form throughout the system, including kink formation and diffusion, as well as simpler motions such as trans–gauche isomerization. These defects allow for effective volume increases (of the defect-containing thiol molecules) and the initiation of laminar curvature, hinging, and cleavage. Concurrent curvature of the metal oxide on the molecular level has shown to be theoretically possible.[47]

An increase in the interlaminar distance only occurs when tightly (chemically) bound water is removed during HT, caused by the well-documented condensation mechanism.[48] The cleavage of the lamina could also be attributed to the shear stress induced by the loss of coordinated water during HT recrystallization from monoclinic to the more distorted orthorhombic V_2O_5,[32] which can accommodate structural distortion and bending. The interlaminar spacing is not observed to change when only bound water, which is reversibly absorbed or hydrogen-bonded, is removed. The condensation forms the driving force behind the hinging observations and, during intercalation, buckling occurs preferentially (with sufficient movement allowance by the organic intercalate in this case) where the pyramidal VO_5 units share only corners (γ-V_2O_5). Heating, even from a 30 kV electron beam cannot be ruled out entirely, but it is unlikely since raising the temperature of an ordered alkanethiol arrangement results in a liquid-like amorphous phase without long-range structural order, whereas, in fact, the opposite is observed. We note that, unlike other vanadate systems, for example, amine-intercalated V_2O_5,[15,49] rolling of the laminar fibers does not occur, but rather site-specific bending and ultimately breakage of the vanadate lamina is observed. The cleaved segments form macroscopic defects in the nanofibers, leaving mainly organic molecule-containing areas segmented periodically by inorganic layers in a bar-coded manner. Where crystalline cleavage does not occur, flexural motion about the hinge is caused by changes in both alkyl-chain conformations and vanadate-unit-cell distortion from a monoclinic to orthorhombic structural phase change, resulting in bending.

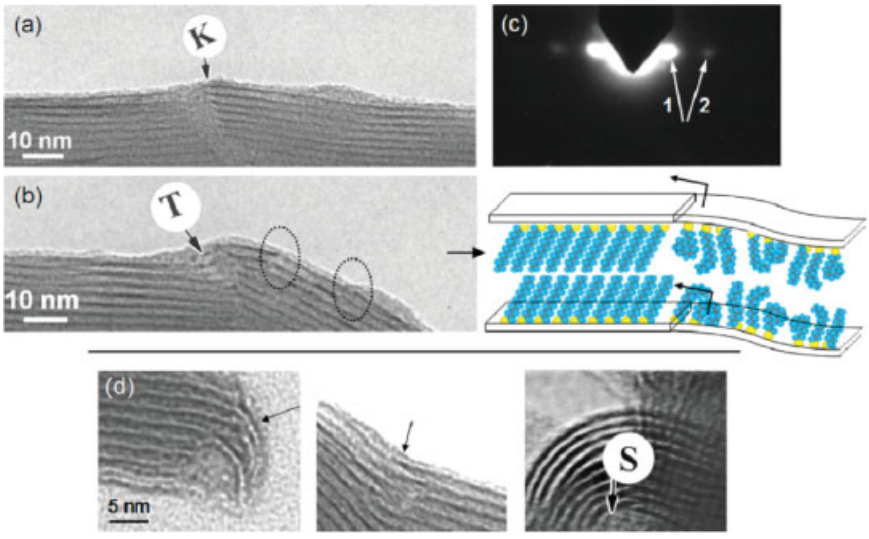

Figure 8. Bright-field TEM images of fully developed VO_x-$(DDT)_{0.27}$ nanofibers acquired at Scherzer (optimum) defocus near a) cleavage and b) bending deformation regions. Lattice planes are clearly resolved through diffraction contrast. The marked oval regions indicate regions where cleavage of the lamina occurs with local removal of thiols. c) Associated SAED pattern of the nanofibers exhibiting 1) a 4.85-nm interlaminar spacing and 2) half-spacing diffraction from the interlaminar molecular bilayer. d) A series of TEM images of various bending and hinging of the nanofiber lamina. The higher scattering S-containing centers contribute to the darker regions (highlighted by arrows) of the interlaminar spacing by diffraction contrast. The schematic indicates the defective liquid-like thiol arrangement at the hinge points, and the arrows indicate directions of shearing.

3. Conclusions

A simple chemical route involving the hydrothermal treatment of dodecanethiol-intercalated vanadium pentoxide xerogel results in the formation of monocrystalline orthorhombic VO_x-$(DDT)_{0.27}$ nanofibers. The highly laminar xerogel readily uptakes alkanethiol molecules between vanadate atomic bilayers. Post-HT XRD and ED studies reveal that the nanofibers are composed of stacked double bilayers of thiol-intercalated VO_x with typical widths of 50–500 nm and lengths typically of 2–6 μm.

An increase in the interlaminar spacing distance is observed after HT because of removal of tightly bound water molecules within the vanadate xerogel, allowing for spectroscopically detectable movement of the all-trans molecular bilayer, which contributes to the observed bending and breakage of the vanadate atomic layers of the nanofibers.

We observe concomitant hinging of the flexible nanofiber lamina at periodic hinge points in the final product on both the nanoscale and molecular level. Bar-coded nanofibers comprise alternating segments of organic–inorganic (thiols–VO_x) material, and under certain conditions free-standing bilayered organic nanostructures are realized, improving on previously reported synthesis methods for such structures. These periodic organic–inorganic structures were shown to dock Au nanoparticles in the vicinity of the thiols. It is plausible that other guest molecules such as quantum dots or biological entities could be systematically arranged in such lamellar systems.

The layered turbostratic structure of the metal oxide nanofibers, when preserved, could provide a new organic templated-synthesis route for the fabrication of multifunctional layered nanostructures that can be functionalized for segmented nanoparticle docking sites, luminescent nanoparticle scaffolds, curved and flexible metal oxides and organic membranes, among other potential applications. With organic bilayers comprising the hinge, vanadium oxide segments can be robustly held together and undergo bending motion about the hinge. In addition to their potential functional capability, the mechanical properties of these nanostructures could allow them to be applied in nanoscale analogues of various types of macroscale machines and devices.

Although the above-described bending motion of these nanofibers is useful as a proof-of-concept idea, in addition to the structural and physical benefits of such materials, controlled bending motion of these bar-coded nanofibers is needed to make them useful for a number of potential applications, such as multifunctional transducer components and nanoscale actuators. However, modifications and extensions of the technique can be anticipated that would enhance its capabilities, as well as potentially extending the range of applications.

4. Experimental Section

The vanadium pentoxide xerogel ($V_2O_5 \cdot nH_2O$) was prepared from monoclinic phase V_2O_5 (Aldrich). A mixture of *t*-butyl alcohol and V_2O_5 was refluxed for 6 h to form the xerogel. Deionised pure water was added to the resulting dark yellow solid and the remaining *t*-butyl alcohol was removed with excess water in vacuum to yield a suspension. The material was aged at room temperature yielding a red-brown colloidal monoclinic V_2O_5. V_2O_5 and the alkyl primary thiol (98%) dodecanethiol (DDT) were stirred in ethanol for 2 h in a molar ratio of 1:1, after which 20 mL of water was added and the resulting solution was agitated for 48 h at 313 K. The VO_x-DDT nanocomposite was transferred to a Teflon-lined autoclave in a sand bath and held at 313 K for several days under auto-generated pressure. Analysis of the product obtained at 313 K: Experimental (calculated) for $C_{27.6}H_{68.8}S_{2.9}O_{9.5}V_2$: C, 44.37 (44.34); H, 9.22 (9.21); S, 12.42 (12.41).

Powder XRD characterization was performed using a Siemens D5000 diffractometer (Cu $K\alpha = 0.15418$ nm, operation voltage 40 kV, current 30 mA). The morphological characterization was performed by FESEM using a JEOL JSM-6700F instrument. TEM and SAED were conducted using a Philips CM300 FEGTEM instrument operating at 30–300 kV. Samples were mounted on holey carbon

grids for structural analysis and on copper grids for EDX measurements. For snap-shot imaging of hinge movement, the accelerating voltage was reduced to 30 kV and a sample mounted directly from HT was imaged at intervals. STM was conducted using a PicoSPM instrument (Molecular Imaging, Inc.). Details on specific conditions and preparations for accurate imaging of adsorbed alkanethiolates can be found in Ref. [50]. The chemical composition of the samples was determined using a SISONS model EA-1108 analyzer. The Fourier transform infrared (FTIR) spectra were recorded using the KBr pellet technique with a Bio-Rad Excalibur model FTS 3000. The XPS measurements were performed in normal emission geometry. A VG CLAM 2 spectrometer and a Mg Kα X-ray source, operating at 250 W, were used several centimeters from the samples. The energy scale was referenced to the Au 4f peak at 84.0 eV.[51] The spectra were normalized to the total electron yield to correct for small differences in sample positions and X-ray source intensities. The resulting spectra were fitted by using a Shirley-type background[52] and symmetric Voigt functions[53] with variable Gauss and Lorentz contributions.

Acknowledgements

The support of Science Foundation Ireland (SFI) under Investigator award 02/IN.1/172, the EU Network of Excellence PhOREMOST (FP6/2003/IST/2-511616), and FONDECyT Grants 1050344 and 1070195 are all gratefully acknowledged. V. L. acknowledges financial support from Rede Nacional de Pequisa em Nanotubos de Carbono (CNPq, Brazil).

[1] P. M. Ajayan, S. Iijima, *Nature* **1992**, *358*, 23.
[2] A. M. Morales, C. M. Lieber, *Science* **1998**, *279*, 208.
[3] Y. F. Zhang, Y. H. Tang, N. Wang, D. P. Yu, C. S. Lee, I. Bello, S. T. Lee, *Appl. Phys. Lett.* **1998**, *72*, 1835.
[4] J. D. Holmes, K. P. Johnston, R. C. Doty, B. A. Korgel, *Science* **2000**, *287*, 1471.
[5] Z. W. Pan, Z. R. Dai, Z. L. Wang, *Science* **2001**, *291*, 1947.
[6] Y. H. Gao, Y. Bando, T. Sato, *Appl. Phys. Lett.* **2001**, *79*, 4565.
[7] Y. N. Xia, P. D. Yang, Y. G. Sun, Y. Y. Wu, B. Mayers, B. Gates, Y. D. Yin, F. Kim, H. Q. Yan, *Adv. Mater.* **2003**, *15*, 353.
[8] P. Gomez-Romero, *Adv. Mater.* **2001**, *13*, 163.
[9] J. F. Xu, R. Czerw, S. Webster, D. L. Caroll, J. Ballato, R. Nesper, *Appl. Phys. Lett.* **2002**, *79*, 1711.
[10] C. Gomez-Navarro, P. J. de Pablo, J. Colchero, Y. Fan, M. Burghard, J. Gomez-Herrero, A. M. Baro, *Nanotechnology* **2003**, *14*, 134.
[11] V. Lavayen, C. O'Dwyer, S. B. Newcomb, M. A. Santa Ana, E. Benavente, G. González, C. M. Sotomayor Torres, *Phys. Status Solidi B* **2006**, *243*, 3285.
[12] V. Lavayen, C. O'Dwyer, G. González, G. Cárdenas, C. M. Sotomayor Torres, *Mater. Res. Bull.* **2007**, *42*, 674.
[13] G. T. Kim, J. Muster, V. Krstic, J. G. Park, Y. W. Park, S. Roth, M. Burghard, *Appl. Phys. Lett.* **2000**, *76*, 1875.
[14] C. O'Dwyer, V. Lavayen, S. B. Newcomb, M. A. Santa Ana, E. Benavente, G. González, C. M. Sotomayor Torres, *J. Electrochem. Soc.* **2007**, *154*, K29.
[15] C. O'Dwyer, D. Navas, V. Lavayen, E. Benavente, M. A. Santa Ana, G. González, S. B. Newcomb, C. M. Sotomayor Torres, *Chem. Mater.* **2006**, *18*, 3016.
[16] C. O'Dwyer, V. Lavayen, S. B. Newcomb, M. A. Santa Ana, E. Benavente, G. González, C. M. Sotomayor Torres, *Electrochem. Solid-State Lett.* **2007**, *10*, A111.
[17] R. Parthasarathy, J. T. Groves, *Soft Matter* **2007**, *3*, 24.
[18] N. Kucerka, J. Pencer, J. N. Sachs, J. F. Nagle, J. Katsaras, *Langmuir* **2007**, *23*, 1292.
[19] R. Parthasarathy, C. Yu, J. T. Groves, *Langmuir* **2006**, *22*, 5095.
[20] A. Roux, D. Cuvelier, P. Nassoy, J. Prost, P. Bassereau, B. Goud, *EMBO J.* **2005**, *24*, 1537.
[21] H. T. McMahon, J. L. Gallop, *Nature* **2005**, *438*, 590.
[22] J. Zimmerberg, M. M. Kozlov, *Nat. Rev. Mol. Cell. Biol.* **2006**, *7*, 9.
[23] A. Hultgren, M. Tanase, C. S. Chen, G. J. Meyer, D. H. Reich, *J. Appl. Phys.* **2003**, *93*, 7554.
[24] S. R. Nicewarner-Peña, A. J. Carado, K. E. Shale, C. D. Keating, *J. Phys. Chem. B* **2003**, *107*, 7360.
[25] M. P. Jonsson, P. Jonsson, A. B. Dahlin, F. Höök, *Nano Lett.* **2007**, *7*, 3462.
[26] W. F. Paxton, A. Sen, T. E. Mallouk, *Chem. Eur. J.* **2005**, *11*, 6462.
[27] G. A. Ozin, I. Manners, S. B. Fournier, A. Arsenault, *Adv. Mater.* **2005**, *17*, 3011.
[28] S.-C. J. Huang, A. B. Artyukhin, J. A. Martinez, D. J. Sirbuly, Y. Wang, J.-W. Ju, P. Stroeve, A. Noy, *Nano Lett.* **2007**, *7*, 3355.
[29] H. Maeda, Y. Maeda, *Nano Lett.* **2007**, *7*, 3329.
[30] A. Ulman, *Chem. Rev.* **1996**, *96*, 1533.
[31] F. Schreiber, *Prog. Surf. Sci.* **2000**, *65*, 151.
[32] O. Durupthy, N. Steunou, T. Coradin, J. Maquet, C. Bonhomme, J. Livage, *J. Mater. Chem.* **2005**, *15*, 1090.
[33] J. Y. Ying, A. Nakahira, D. M. Antonelli, *Inorg. Chem.* **1996**, *35*, 3126.
[34] J. Livage, *Chem. Mater.* **1991**, *3*, 578.
[35] V. Lavayen, M. A. Santa Ana, J. Seekamp, C. M. Sotomayor Torres, E. Benavente, G. González, *Mol. Cryst. Liq. Cryst.* **2004**, *416*, 49.
[36] N. Pinna, M. Willinger, K. Weiss, J. Urban, R. Schögl, *Nano Lett.* **2003**, *3*, 1131.
[37] V. Petkov, P. Y. Zavalij, S. Lutta, M. S. Whittingham, V. Paranov, S. Shastri, *Phys. Rev. B* **2004**, *69*, 085 410.
[38] M. J. Hostetler, J. J. Stokes, R. W. Murray, *Langmuir* **1996**, *12*, 3604.
[39] W. Chen, Q. Mai, J. F. Peng, Q. Xu, Q. Y. Zhu, *J. Mater. Sci.* **2004**, *39*, 2625.
[40] X. Chen, X. Sun, Y. Li, *Inorg. Chem.* **2002**, *41*, 4527.
[41] J.-S. Yu, J. Y. Kim, S. Lee, J. K. N. Mbindyo, B. R. Martin, T. E. Mallouk, *Chem. Commun.* **2000**, 2445.
[42] G. Decher, *Science* **1997**, *277*, 1232.
[43] C. D. Keating, M. J. Natan, *Adv. Mater.* **2003**, *15*, 451. S. R. Nicewarner-Peña, G. P. Freeman, B. D. Reiss, L. He, D. J. Peña, I. D. Walton, R. Cromer, C. D. Keating, M. J. Natan, *Science* **2001**, *294*, 137.
[44] H. A. Müller, M. Zharnikov, B. Volkel, A. Schertel, P. Harder, M. Grunze, *J. Phys. Chem. B* **1998**, *102*, 7949.
[45] S.-M. Lee, S.-N. Cho, J. Cheon, *Adv. Mater.* **2003**, *15*, 441.
[46] W. Mar, M. L. Klein, *Langmuir* **1994**, *10*, 188.
[47] N. Seriani, Z. Jin, W. Pompe, L. Colombi Ciacchi, *Phys. Rev. B* **2007**, *76*, 155 421.
[48] J. Livage, M. Henry, C. Sanchez, *Prog. Solid-State Chem.* **1988**, *18*, 259.
[49] F. Krumeich, H.-J. Muhr, M. Niederberger, F. Bieri, B. Schnyder, R. Nesper, *J. Am. Chem. Soc.* **1999**, *121*, 8324.

[50] C. O'Dwyer, G. Gay, B. Viaris de Lesegno, J. Weiner, *Langmuir* **2004**, *20*, 8172.
[51] J. F. Moulder, W. E. Stickle, P. E. Sobol, K. D. Bomben, *Handbook of X-ray Photoelectron Spectroscopy* (Ed.: J. Chastian), Perkin-Elmer Corporation, Eden Prairie, MN 1992.
[52] D. A. Shirley, *Phys. Rev. B* **1972**, *5*, 4709.
[53] G. K. Wertheim, M. A. Butler, K. W. West, D. N. E. Buchanan, *Rev. Sci. Instrum.* **1974**, *45*, 1369.